Journal of The
Electrochemical Society

Understanding the Role of Microstructure in the Extraction of Solid-State Diffusion Coefficients by a 3D Modeling Approach

Journal of The Electrochemical Society, 2026 **173** 130503

Understanding the Role of Microstructure in the Extraction of Solid-State Diffusion Coefficients by a 3D Modeling Approach

Johannes Hörmann,[1,2] Yannick Kuhn,[1,2] Simon Hein,[1,2] Birger Horstmann,[1,2,3] Timo Danner,[1,2,z] and Arnulf Latz[1,2,3]

[1]*German Aerospace Center (DLR), Institute of Engineering Thermodynamics, 70569 Stuttgart, Germany*
[2]*Helmholtz Institute Ulm for Electrochemical Energy Storage (HIU), 89081 Ulm, Germany*
[3]*Ulm University, Institute of Electrochemistry, 89081 Ulm, Germany*

For insertion-type lithium-ion batteries, the solid-state diffusion coefficient of Li^+ in an active material is considered a key parameter within the research community. The capabilities and limits of related parameter extraction methods are usually well-established. However, there is a gap in understanding the influence of the applied measurement setup. In practice, many setups unintentionally violate the assumptions of the extraction method. We apply the galvanostatic intermittent titration technique (GITT) in virtual experiments using 3D microstructure-resolved simulations in varying model measurement setups. Diffusion coefficients are extracted by applying a state-of-the-art Bayesian optimization approach which is particularly suitable for non-uniquely solvable problems. The investigated parameters are within the typical literature range of $LiNi_{0.8}Mn_{0.1}Co_{0.1}O_2$ (NMC811). Because experimental boundary conditions are precisely known within the simulation setups, the influence of microstructural features on the extracted diffusion can be isolated and quantified. The investigation shows, that the applied monodisperse thin-electrode and single-particle setup are capable of extracting the actual diffusivity with up to 4% and 17% point-estimate deviation, respectively. Particle cracking proved to have the largest impact on extracted diffusion coefficients. Nevertheless, all predictions remained close to the correct order of magnitude, i.e. point estimates deviated at most by factors in the range of $10^{\pm 0.88}$.
 [DOI: 10.1149/1945-7111/ae7cb8]

Manuscript submitted March 12, 2026; revised manuscript received May 29, 2026. Published July 1, 2026.

Supplementary material for this article is available online

The active material (AM) plays a key role in determining the energy density as well as performance of a battery. The theoretical specific energy density of a material represents the thermodynamic limit for a certain AM chemistry. However, the actual performance of an AM in a full battery system is influenced by many more factors. Particularly, the AM has to be able to provide certain electrochemical performance metrics depending on the operating conditions. Such requirements depend on the surrounding electrode structure and application case of a battery. In contrast, the capabilities of an AM are determined by the type of AM and its inherent microstructure, which can be quantified by electrochemical characterization. In order to compare the suitability and potential of different AMs when designing a battery, the related characterization methods need to be reliable and precise. This is also crucial for enabling the tuning and optimization of AM microstructure to intended application cases by means of particle design.[1] Further, most quantities used to characterize AM properties also directly relate to input parameters required for battery modeling. Improving the accuracy and reliability of parameters is therefore also intriguing for enhancing the accuracy of model predictions and creating digital twins of batteries.

Characteristic properties of AMs for Li-ion batteries (LIBs) are typically the solid-state diffusion coefficient D_{Li} of the charge carriers, i.e. Li^+, the electronic conductivity σ_s, and the charge-transfer resistance R_{CT}. The latter can be related to the exchange current density i_0. Together with the other two quantities it is commonly used in order to describe AM-related transport in battery modeling.[2–5] This work will focus on the determination of D_{Li}, which is a key parameter for the rate-capability of an AM. Many experimental methods are reported in the literature for its extraction. They include the galvanostatic intermittent titration technique (GITT),[6] the potentiostatic intermittent titration technique (PITT),[7] the intermittent current interruption (ICI) method,[8] and electrochemical impedance spectroscopy (EIS).[9] Fundamentally, these methods all rely on the same principle by starting from global equilibrium or steady-state. Then, the AM is perturbed out of its equilibrium condition by a change of current or voltage while measuring the other variable as a function of time. As a final step, an appropriate model has to be applied to extract D_{Li} from the data.

Electrode systems built for AM characterization are typically designed to minimize influences of the electrode's structure. This can be achieved by thin electrode sheets with conductive additives which can even go down to single-layer sheets.[10] An alternative approach measures single material particles via so-called single-particle measurements (SPM).[11,12] Models for the extraction of D_{Li} from the data have also been evolving since the first introduction of the Weppner-Huggins (WH) formula for GITT.[6] The method's shortcomings have been analyzed and application standards established.[13] Many flaws arising from strong model assumptions in the original work have been tackled leading to more generally applicable and accurate methods.[14–18] Apart from improved accuracy, some advanced methods like ICI offer significant reduction of experiment time.[8,19] Among these methods, approaches based on Bayesian optimization stand out.[20] They are suitable for parameter extraction as well as battery model parameterization in general. In particular, these approaches are not bound to a specific experimental technique. Furthermore, they are especially suitable for non-uniquely solvable problems while offering the significant advantage of estimating the precision of extracted parameters.[18,20] Nevertheless, the combination of GITT with the WH-formula, also known as four-point formula, is still very common in literature due to its simplicity.[13]

Solid-state diffusion coefficients reported for a single type of AM often span several orders of magnitude in the literature. For LIBs this concerns popular negative as well as positive electrode materials. For example, Wang et al.[21] reported values in the range of 10^{-13} cm^2/s and 10^{-7} cm^2/s for graphite and Günther et al.[10] values ranging from 10^{-12} cm^2/s to 10^{-8} cm^2/s for NMC622. The usage of evaluation methods with intrinsic model imprecisions is, however, only one reason for the reported wide variance. There are several other possible explanations for these deviations. On the one hand, this comprises electrode designs or measurement procedures not suited for the applied parameter extraction method. On the other hand, there remain various unavoidable influencing factors. First, there is a

[z]E-mail: timo.danner@dlr.de

remaining influence of any measurement setup even under optimal conditions. Electrode-scale measurements are influenced by partial surface coverage due to conductive additives as well as inter-particle contact. Furthermore, AM particles commonly do not have a monodisperse particle size distribution (PSD). Measurements in SPM setups usually operate without conductive additives leading to stronger influences of an AM's electronic conductivity and connectivity. Second, there is an influence of the microstructure of the AM, which can be quite complex. For NMC-type materials, many microstructural features can be tuned by advanced production methods including the grain structure,[22] porosity,[23] and local chemical composition.[24] Understanding the precise effects of these microstructural features on the electrochemical dynamics remains a challenge of ongoing research. For practical AM classification, state-of-the-art parameter extraction therefore typically assumes that the AM is a homogeneous material. Microstructural effects are, thus, compressed into a single diffusion constant D_{Li}. Particle cracking is a classical example demonstrating how these model assumptions break down during the measurement procedure. It is typical for polycrystalline NMC-type materials.[25] In this particular case active surface area and electronic path length increase. Meanwhile, diffusional pathways in the AM decrease since transport of Li toward the particle center is improved by electrolyte invading the particle cracks. Ruess et al.[26] investigated this effect by performing GITT measurements on electrodes of similar loading with both liquid and solid electrolytes (SE). Compared to the solid case, they observed an apparent increase in D_{Li} in the liquid case exceeding one order of magnitude. Nevertheless, distinguishing and quantifying effects of microstructural electrode and particle features on the extracted solid-state diffusion coefficient remains challenging. In experiments, effects typically overlap with each other and are hard to quantify precisely. Combining 3D electrochemical simulations with parameter extraction methods can aid in tackling these challenges. These so-called virtual experiments have the distinct advantage, that the microstructural and electrochemical conditions can be controlled precisely. Nevertheless, there are only limited results utilizing the approach in the literature so far. The method allows for example to isolate microstructural electrode features and quantify the resulting uncertainty in the extraction process. Performing virtual experiments combined with the four-point formula, Chouchane et al.[27] investigated the effect of a carbon-binder domain (CBD) prohibiting electrolyte transport.

In this work, we conduct virtual GITT experiments on spherical NMC811 AM via 3D microstructure-resolved simulations. By creating virtual structures, the effect of specific microstructural features can be isolated and observed. Thereby, we obtain virtual GITT measurement data showing how the measured voltage curves are expected to change due to certain features. This information is complemented by 3D-resolved information on the dynamics allowing for physics-based explanations of the observed voltage curves. Further, we extract D_{Li} from the virtual GITT measurement data using a Bayesian optimization approach. By that, the resulting deviations of the measured D_{Li} can be quantified by comparing it to the intrinsic value of the AM used as input to our simulations.

The applied methods are explained in the following section starting with details on the virtual GITT experiments, including the applied continuum modeling approach and virtual structures. Then, the employed parameter extraction methods are explained. The main part of this work starts by verifying the applied setup followed by detailing the impact of various microstructural features including AM connectivity, secondary particle structure, and electrode microstructure. To complete the picture, the employed parameter extraction method is compared to other evaluation methods including the common extended WH-formula. Finally, the results are complemented by a summary and conclusion.

Methods

The methods required for the complete workflow for virtual active material testing depicted in Fig. 1 is detailed in the following. Virtual GITT experiments are conducted on varying setups (Fig. 2) with a known intrinsic D_{Li}, which is combined with the parameter extraction methods explained within this section. By this, the observed errors in the determined effective chemical diffusion coefficients can be linked to uncertainties introduced by the setup and complemented with physical explanations.

***Virtual GITT experiments.*—**For the conduction of virtual GITT experiments in a SPM setup as well as different electrode configurations, we use the simulation framework *BEST*.[28] Its finite volume implementation of a microstructure-resolved electrochemical battery model gives precise control over the microstructure in each virtual measurement scenario. This includes the particle structure as well as the connection of particles to their surrounding, that is the current collector in the SPM setup as well as other AM particles in the electrode configurations. The different measurement setups will be explained in detail after first introducing the model.

Model description.—The transport model is based on a previously established continuum modeling approach. The full system of PDEs describing the model can be derived from general principles of non-equilibrium thermodynamics, which is detailed in Refs. 3, 29. The model describes the spatial and temporal evolution of temperature, concentrations, and potentials. More precisely, the lithium-ion concentration and electrical potential in the solid phases, as well as lithium-ion concentrations and electrochemical potentials in the electrolyte. Typically, GITT measurements are performed using moderate currents. We therefore assume a constant temperature in the simulations leading to the set of governing Equations detailed in Table S3. Note, that the model allows to spatially resolve the current

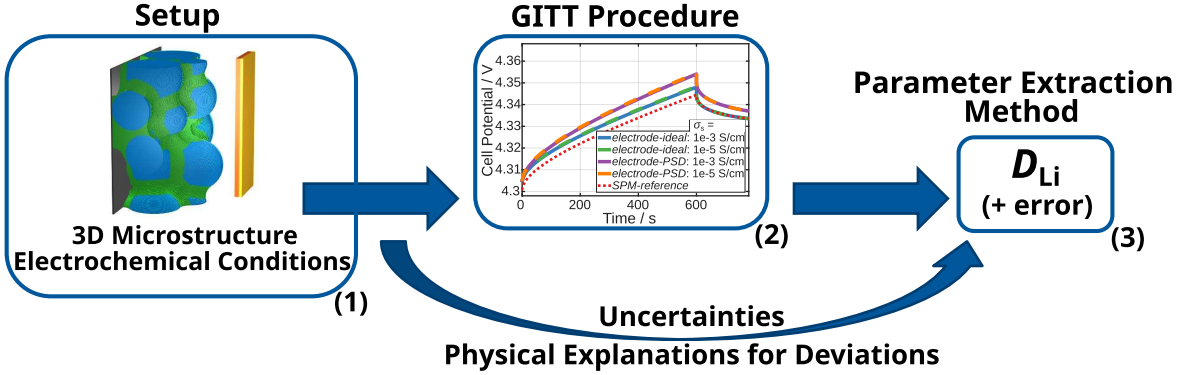

Figure 1. The applied virtual active material testing workflow. The virtual measurement setup (1) requires a 3D microstructure and the parameters defining the electrochemical conditions. A virtual GITT measurement (2) is performed on the setup by applying the continuum modeling approach detailed in the Methods section. Based on the fully available microstructural information and the known intrinsic D_{Li}, physical explanations for the observed errors and uncertainties in the parameter extraction (3) can be given.

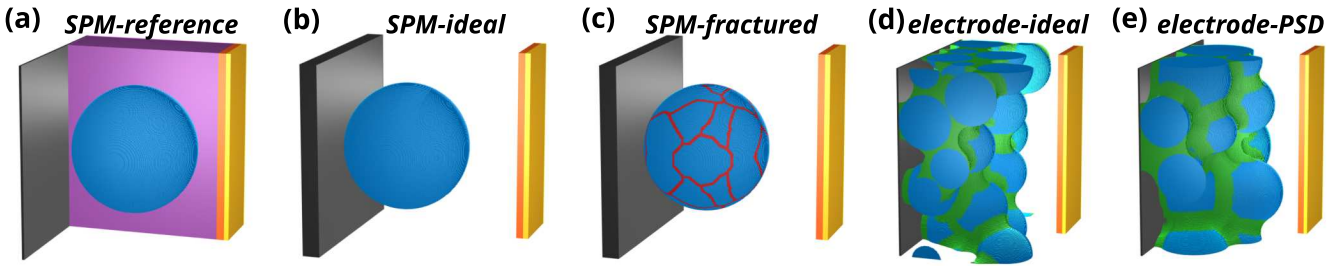

Figure 2. Model geometries used for the virtual GITT experiments. The CCs are depicted in black, the AM in blue, and the CBD in green. The void space is occupied by the electrolyte. The Li-metal counter electrode (yellow) and separator (orange) are only shown in the back third of each illustration. Their actual thickness in through-direction is rescaled for a better visualization. Similarly, the fictional embedding material in the *SPM-reference* case (purple) is only shown in the back third. The cracks in the *SPM-fractured* case are filled with electrolyte and highlighted in red.

collectors. For an accurate representation of electrodes which are typical for GITT measurements, it is necessary to include the effects of conductive additives and binders in the model. Therefore, we assume that the two materials can be described as a homogeneous, porous material filled with electrolyte. The intricate microstructure is beyond the scale of resolution. Hence, the CBD is modeled using mathematical homogenization approaches resulting in effective transport parameters for ions and electrons. A complete list of all parameters used in the virtual experiments is given in Table S4. The parameters for the active material were varied to investigate their impact on electrochemical measurements and particularly on extracted chemical diffusion coefficients. They are listed in Table I and are in the typical range of literature values for NMC811.[8,26,30,31] As a consequence, the parameter variation also accounts for uncertainties regarding the solid-state diffusion coefficient and electronic conductivity of NMC811. Further information on the applied model is provided in Section S1. The low sensitivity with respect to the intercalation rate i_0 was also checked and is discussed in Section S7.

Simulation geometries.—In order to discern the effects of specific microstructural features in virtual GITT measurements, five different electrode microstructures were investigated. The different setups are depicted in Fig. 2. Additional statistical information like their capacity and surface area are detailed in Fig. S3.

The setup in Fig. 2a ("*SPM-reference* case") serves as a baseline for the investigation. It allows a validation of the virtual experiment as well as the parameter extraction methods for the solid-state diffusion coefficient D_{Li}. The spherical particle within the setup has a diameter d_{P} of 13 μm and is embedded into a highly porous and conducting material. The structure has a Li-metal counter electrode and a separator, which consists of pure electrolyte with a thickness of 400 μm. We want to emphasize, that the surrounding material for the embedding is fictional and its whole purpose is to create a reference setup. The setup emulates homogenized cell-scale models like the Doyle-Fuller-Newman (DFN) model or single-particle models.[2,5] As these models make similar simplifying assumptions, the *SPM-reference* case yields solutions that can be directly compared. Furthermore, the applied extraction methods for D_{Li} detailed below can be validated. This is possible, since a variant of the single-particle model was chosen in the approach based on Bayesian optimization.

The setup in Fig. 2b ("*SPM-ideal* case") also features a single spherical particle with $d_{\mathrm{P}} = 13$ μm. The particle is partly embedded (0.40625 μm) into the current collector (CC) relating to an angle of 45° between two opposite edges of the covered spherical cap. The rest of the particle surface is exposed to the electrolyte. The separator is the same as in the *SPM-reference* case. Thereby, the setup allows the investigation of effects due to electrical particle contact and connectivity. Moreover, the setup mimics typical conditions of a single-particle measurement.[11]

Figure 2c ("*SPM-fractured* case") is the same as the *SPM-ideal* case except that the sphere in addition exhibits cracks. The randomly distributed cracks align with the radial direction of the particle and reach a depth of roughly 4 μm. They are filled with electrolyte and their different color in Fig. 2c is only for illustrative purposes. The crack structure is shown in detail in Fig. S3(b).

The electrode setup in Fig. 2d ("*electrode-ideal* case") is designed to exhibit ideal conditions for a GITT measurement on an electrode. The monodisperse ($d_{\mathrm{P}} = 13$ μm) and approx. 20 μm thick electrode has around 51.13 vol% active material and 14.75 vol % CBD. For NMC811, this relates to a mass ratio of 90:5:5 (NMC: carbon:binder) and a mass loading of 5.531 mg/cm^2. The electrode was generated by piling grains in a periodic structure until the target volume fraction was reached using the software GeoDict.[32] Subsequently, CBD was distributed within the electrode structure by applying a standard morphological closing algorithm.[33,34] The electrode's Li-metal counter electrode is placed on top of a 25 μm thick separator of type Celgard 2325.[35] The setup allows to analyze the influence of conductive additives and binders as well as a comparison between a SPM and an electrode consisting of many particles.

Finally, the electrode setup depicted in Fig. 2e ("*electrode-PSD* case") is similar to Fig. 2d, but the particles were drawn from a Gaussian distribution with mean diameter $d_{\mathrm{P}} = 13$ μm. It was created by the same procedure as detailed for the *electrode-ideal* case, but the particles in the piling algorithm were drawn randomly from a distribution. Detailed information on the distribution and particle sizes is provided in Fig. S4. The electrode contains around 49.49 vol% active material and 15.49 vol% CBD. For NMC811, this relates to a mass ratio of 90:5:5 (NMC:carbon:binder) and a mass loading of 5.400 mg/cm^2.

GITT procedure.—The GITT measurement protocol applied in all of the virtual experiments consisted of two phases. During the initial pulse phase, a constant current of 0.1 C is applied for a duration of 600 s followed by a rest period at zero current for 6 hours. The initial concentration of lithium in the active material at the beginning of the procedure was set to 0.010312 mol/cm^3. This concentration corresponds to a degree of lithiation of 20.60% and an open-circuit potential of 4.300 V. The C-rate was calculated based on the maximum concentration of lithium $c_{\mathrm{s,max}} = 0.05006$ mol/cm^3 assuming a utilization of 80%. Consequently, this results in a total change of degree of lithiation equal to 1.333% for all setups and the applied current corresponds to 27.55 mA/g for NMC811.

Parameter extraction methods.— *Bayesian optimization approach.*—For a precise extraction of solid-state diffusion coefficients from GITT measurement data, we employ a Bayesian optimization approach ("EP-BOLFI"). The previously established method extends

Table I. Parameters for the active material used in the simulation study. Values are in the typical range of parameters for NMC811.

D_{Li} (cm^2/s)	10^{-12}, 10^{-11}, 10^{-10}
σ_{s} (S/cm)	10^{-5}, 10^{-4}, 10^{-3}
i_0 (A cm/mol)	0.23047 (Ref. [30])

Bayesian Optimization (BOLFI) with Expectation Propagation (EP) for likelihood-free inference to create an efficient black-box optimizer.[18] A key trait of this approach is, that the measurement data is divided into physics-based features instead of fitting the data as a whole. This allows to incorporate knowledge about the underlying physics of the process into the parameter extraction process and speeds up the algorithm significantly. A cell-scale battery model can hence be used by the algorithm and is fit directly to the features. The battery simulations are carried out using the efficient open source tool *PyBaMM*.[36] While the method itself has been shown to be capable of fitting a multitude of unknown parameters at once, it will be used to only extract solid-state diffusion coefficients here. In order to facilitate the fitting process, the intercalation rate of the active material is used as a second free parameter. This additional degree of freedom yields the advantage, that no previous knowledge of the active surface area has to be assumed in the process. EP-BOLFI was applied with a fixed optimizer setting to all configurations, inserting the least amount of bias into the extraction process. In order to realize this in conjunction with noise-free simulated data, EP was disabled in the algorithm. It should be emphasized, however, that this is only recommended for noise-free data and expectation propagation is a key component of the algorithm when working with noisy data.[18] A single-particle model with a correction term accounting for the electrolyte behavior (SPMe) was chosen as a battery model for the fitting procedure.[5] This model closely matches the conditions in the *SPM-reference* case. Furthermore, the electrode structures consist of only a thin electrode layer with a sufficient amount of conductive additives for percolating electronic pathways, such that transport limitations can be neglected. Hence, more detailed cell-scale models like DFN do not improve accuracy of the method in a noticeable way.[37] For the choice of the physics-based features, we incorporate five features following Kuhn et al.[18] For the pulse phase, we chose the initial voltage $U^{\mathrm{P}}(t_0)$ by square-root extrapolation as well as the square-root slope $\mathrm{d}U^{\mathrm{P}}/\mathrm{d}\sqrt{t}$ together with the exponential relaxation time τ^{P}. Similarly, $U^{\mathrm{R}}(t_0)$ and $\mathrm{d}U^{\mathrm{R}}/\mathrm{d}\sqrt{t}$ were selected for the relaxation phase. Note, that the initial voltages incorporate information regarding the internal cell resistance, intercalation rate, and concentration overpotential. Both square-root slopes contain direct information on the solid-state diffusion coefficient D_{Li}. This becomes evident via Eq. 1, as the formula also applies to the relaxation phase, where it is called the ICI method.[8] Finally, the relaxation time τ^{P} includes information on the system during prolonged pulse times complementing the short-time square-root fit. The functions used for the fits are given by

$$f^{\mathrm{sqrt}}(t) = U(t_0) + \mathrm{d}U/\mathrm{d}\sqrt{t}\cdot\sqrt{t - t_0}\,,$$
$$f^{\mathrm{exp}}(t) = U(t_0) + \Delta U\cdot\exp\left(-\tau^{-1}\cdot(t - t_0)\right),$$

where t_0 refers to the starting time of the pulse or rest phase. The cell potential plotted over the square root of time in the *SPM-reference* case exhibited approximately linear behavior for the first 180 s of the pulse phase. The square-root fits were restricted accordingly to the first 180 s of each phase. The exponential fit was then restricted to the last 360 s of the total pulse time of 600 s, where the cell potential in the *SPM-reference* case deviated clearly from the square-root-like behavior. The prior 95% confidence intervals for the parameters in the optimization algorithm were chosen to be $D_{\mathrm{Li}} \in$ (8e-13, 5e-10) cm^2/s and $i_0 \in$ (0.01, 10) A cm/mol. These indicate the ranges where the algorithm tries to find optimal parameter values. The ranges were chosen to deliberately cover all real parameter combinations, i.e. the a priori set values in the virtual experiments, with a clear margin. Therefore, EP-BOLFI can be applied to all virtual GITT measurement data with the same settings similar to real conditions for a parameter extraction without previous knowledge of the true values. Fig. 3 depicts exemplary GITT measurement data and illustrates the various chosen features together with the prior 95% confidence intervals. After the application of the optimization algorithm, most-likely parameters are obtained together with their 95% confidence intervals CI_{95}. These

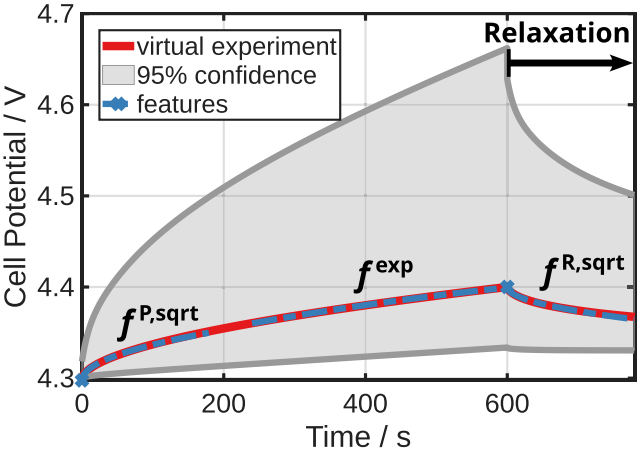

Figure 3. Feature-based parameter extraction via EP-BOLFI. The varying features defined in the Methods section are depicted as dashed blue lines for the exemplary data (red).

intervals reflect the posterior uncertainty from the optimizer providing error bars for the extracted optimal parameters. Further information on the settings of EP-BOLFI is provided in Section S2. A complete list of the extracted optimal D_{Li} with error bounds for the discussion within this work is given in Table S7. The related features as well as the features extracted from the GITT data, are stated in Table S8 and Table S9, respectively.

Weppner-huggins approach.—For the complementary analysis below by a comparison to other evaluation methods, we applied the more general version of the well-known Weppner-Huggins formula,

$$D_{\mathrm{Li}} = \frac{4}{\pi}\left(\frac{V}{A}\frac{\Delta U_0/\Delta t^{\mathrm{P}}}{\mathrm{d}U^{\mathrm{P}}/\mathrm{d}\sqrt{t}}\right)^2. \qquad [1]$$

Therein, V denotes the total volume of the electrode's active material and A the electrochemical active surface area of the electrode. ΔU_0 describes the total change in open-circuit potential during the pulse time Δt^{P}.[6] For the results based on the measured surface areas ($D_{\mathrm{Li}}^{\mathrm{M}}$), the active surface areas of each setup were calculated directly from the microstructures. For the extraction using approximated surface areas ($D_{\mathrm{Li}}^{\mathrm{A}}$), the surface-to-volume ratio of a perfect sphere of radius r_{P} was applied, i.e. $A/V = 3/r_{\mathrm{P}}$. The change in open-circuit potential ΔU_0 was calculated based on the total transferred charge. This mirrors an idealized environment with infinite relaxation time therefore neglecting uncertainties introduced by this factor.

Results and Discussion

In the main part of this section we will discuss the results of the virtual GITT measurements and the subsequently extracted solid-state diffusion coefficient by EP-BOLFI. In particular, we will investigate how microstructural properties change the electrochemical response and determined effective chemical diffusion coefficients. Local changes in the active material's lithiation dynamics can be directly observed and linked to shifts in the measured cell voltage of the virtual GITT experiment. Changes in the voltage in turn translate to deviations in the extracted D_{Li} from the true diffusivity of the material. The discussion in this Section will focus on $D_{\mathrm{Li}} =$ 1e-10 cm^2/s, but the results are also transferable to other values for D_{Li}. A complete discussion on $D_{\mathrm{Li}} =$ 1e-11 cm^2/s and $D_{\mathrm{Li}} =$ 1e-12 cm^2/s is given in Section S6. The influence of the intercalation rate was rather small which is argued in Section S7. First, we will discuss the verification of the extraction workflow which yields a reference for the accuracy of the workflow in other measurement scenarios. Then, different microstructural features will

be investigated. Finally, the results for D_{Li} will be compared to other parameter extraction methods in order to complete the picture.

Verification of workflow.—First, we demonstrate the validity of the workflow using the *SPM-reference* case. This setup can be compared directly to the SPMe model which serves as a cell-scale simulator within the parameter extraction process via EP-BOLFI. Importantly, this process also yields a reference that can be used for comparison throughout the analysis of the varying microstructural features in the following. Fig. 4a shows the lithium concentration within the AM particle. As expected the lithiation shows a radially symmetric pattern. The lithium concentrations are illustrated using the change in degree of lithiation with respect to the initial concentration at the start of the pulse. This quantity will be used throughout the manuscript and is defined by

$$\Delta\mathrm{DoL} = (c_{\mathrm{s}}(t) - c_{\mathrm{s}}(t=0))/c_{\mathrm{s,max}}.$$

Recall, that the average of the total change of ΔDoL equals -1.333% for all setups. For better comparability of the results, lithiation patterns and overpotential distributions will always be depicted at $t = 240$ s.

The good agreement between the SPMe simulation and the *SPM-reference* case with identical parameters can be seen in Fig. 4b. The cell voltages deviate by at most 0.565 mV. The extracted D_{Li} in Fig. 4d shows a small point-estimate deviation of 1.6% from the intrinsic diffusivity in the virtual experiments. This sets a reference for D_{Li} and quantifies the extent of the systematic error mostly due to the voxelization of the spherical particle in the virtual experiment. While it is not the focus of this work to analyze the differences between cell-scale simulations like SPMe and the employed microstructure simulation tool *BEST* in-depth, one needs to be highlighted in particular. Voxel discretization of a perfect sphere, as intended in the *SPM-reference* case, introduces a systematic local fluctuation of the particle surface regardless of resolution, i.e. voxel size. The sphere's volume in turn can be approximated to arbitrary precision. As can be seen in Fig. 4, this does not lead to an incorrect prediction of the cell potential, lithiation pattern or average overpotential. Instead, it introduces a wave-like shape to the overpotential depicted in Fig. 4c as a slice-average going from CC to separator. Additional information on the negligible influence of the voxelized surfaces is provided in Fig. S7. The dependence of simulation results on the applied resolution was investigated in Fig. S5 and found to be minor. In general, the sensitivity of cell potentials with respect to resolution increased with decreasing diffusivity. This resulted in a minor but increasing setup error, which is discussed in Section S6. Further, the influence of electrolyte transport and the lithium counter electrode was investigated. The results are visualized in Fig. S6 showing that their impact is negligible in all virtual setups.

Influence of connectivity.—Now, we will look at the influence of connectivity by means of the *SPM-ideal* case. Changes compared to the *SPM-reference* case originate from partial surface coverage on the one hand and ohmic effects due to a limited electronic connection on the other. By varying the conductivity in the virtual experiments, these two effects can be discerned.

Effect of partial surface coverage.—Figure 5a shows the lithium distribution within the particle for the highest electronic conductivity $\sigma_{\mathrm{s}} = 1\text{e-}3$ S/cm. The pattern is mostly radially symmetric similar to the *SPM-reference* case except for the zone close to the contact with the CC. The corresponding GITT measurement predicted by the simulation is depicted in Fig. 5c and is almost identical to the *SPM-reference* case with a deviation below 0.6 mV. The total surface coverage of the particle covered by the CC is around only 3.093%. Note, that this amount of surface coverage leads to a sufficient electronic connection, which is argued in Section S3. Due to the high electronic conductivity of the active material in this scenario, the influence of ohmic effects is negligible. Differences in the measured voltages by GITT between the *SPM-ideal* case and the *SPM-reference* case are therefore governed by effects due to differing intercalation surface areas. A reduced active surface leads to an increase in the effective current density on the active surface in contact with the electrolyte. This raises the average overpotential and decreases the surface concentration of lithium.

The average overpotential is approximately inversely proportional to the surface area exposed to the electrolyte. The exact relation is discussed in Section S4 and requires sufficiently small currents, which is a reasonable assumption for the applied GITT procedure. This matches with the overpotentials, which are depicted as vertical lines in Fig. 5e, where $6.4878\text{e-}4/6.2702\text{e-}4 \approx 1.0347$ is close to the surface fraction $(1 - 3.093\%)^{-1} \approx 1.0319$. Nevertheless, this is a minor effect as it accounts for only around 0.022 mV deviation in measured voltage.

The second effect, i.e. a stronger decrease in surface concentration, translates to a faster shift of the open-circuit potential compared to the *SPM-reference* case. The effect increases over the pulse duration and mainly causes the voltage differences between the two cases. It amounts already to roughly 0.45 mV after the 240 s pulse duration depicted in Fig. 5. This is consistent with the approximate upper bound, given by

$$\left(\frac{A_1}{A_2} - 1\right) \cdot (U_{\mathrm{meas}}(t^{\mathrm{P}}) - U_{\mathrm{meas}}(0)) \approx 0.0319 \cdot 0.0437 \quad \mathrm{V} \approx 1.4\ \mathrm{mV}. \qquad [2]$$

The derivation and exact assumptions of this approximation are detailed in Section S5.

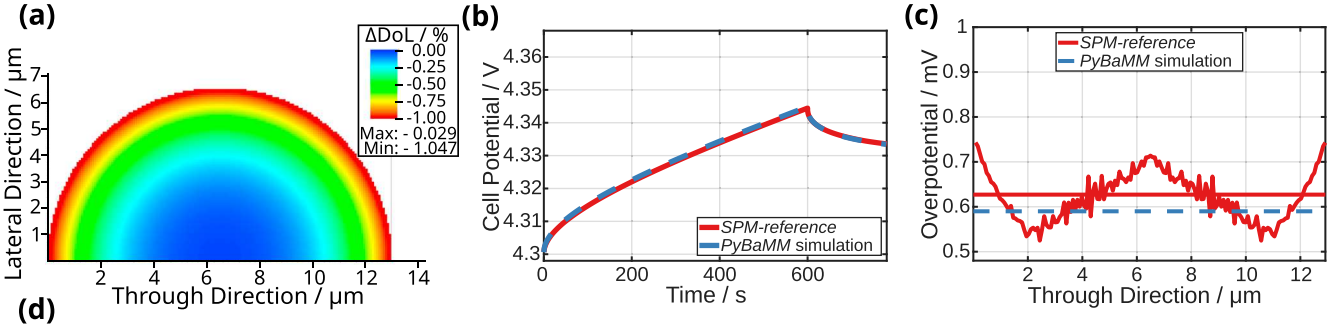

σ_{s} (S/cm)	D_{Li} (1e-10 cm²/s)	CI_{95} (1e-10 cm²/s)
–	0.984	(0.594, 1.629)

Figure 4. Verification of workflow. Results depicted for the *SPM-reference* case with $D_{\mathrm{Li}} = 1\text{e-}10$ cm²/s. (a) Lithiation pattern within the particle at $t = 240$ s with an average ΔDoL of -0.533%. (b) Resulting cell potential for the first 780 s of the GITT procedure. (c) Slice-averaged overpotentials over the through-direction. Horizontal lines indicate global averages. (d) Extracted D_{Li} and 95% confidence CI_{95}.

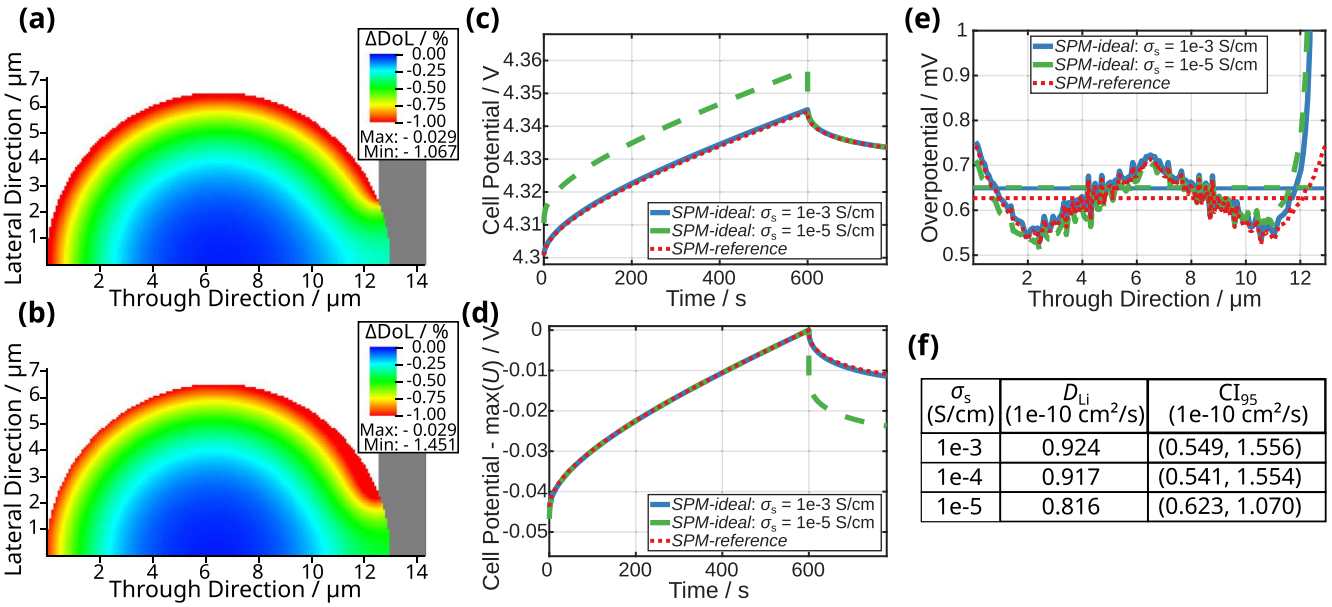

σ_s (S/cm)	D_{Li} (1e-10 cm²/s)	CI_{95} (1e-10 cm²/s)
1e-3	0.924	(0.549, 1.556)
1e-4	0.917	(0.541, 1.554)
1e-5	0.816	(0.623, 1.070)

Figure 5. Influence of connectivity. Results depicted for the *SPM-ideal* case with D_{Li} = 1e-10 cm^2/s. Lithiation pattern within the particle at t = 240 s with an average ΔDoL of −0.533% for (a) σ_s = 1e-3 S/cm and (b) σ_s = 1e-5 S/cm. (c) Resulting cell potentials for the first 780 s of the GITT procedure. (d) Cell potentials shifted by their respective maxima removing constant offsets during the pulse phase. (e) Slice-averaged overpotentials over the through-direction. Horizontal lines indicate global averages. (f) Extracted D_{Li} and 95% confidence CI_{95}.

In summary, the deviation in measured potential during GITT from the *SPM-ideal* case to the *SPM-reference* case for σ_s = 1e-3 S/cm is governed mostly by the fraction of available surface area leading to a shift in surface concentration. Since the available surface area is reduced by less than 4%, the effects on the potential curve are in the same order. It can be argued, that in a real measurement environment this effect will be in the order of magnitude of noise in the measurements or other uncertainties in the experiment.

Effect of conductivity.—The single contact in the SPM setup causes an offset in the cell voltage due to the bottleneck at the contact area. Furthermore, it leads to a shift in the overpotential distribution on the surface due to the variation of path lengths. These effects become relevant at low conductivities and add to the ones caused by partial surface coverage, which were discussed previously. We will look at this by the means of the *SPM-ideal* case with σ_s = 1e-5 S/cm. The related lithium distribution for t = 240 s is depicted in Fig. 5b showing a shift in the lithiation pattern compared to Fig. 5a. Intercalation occurs preferentially closer to the electronic connection at the CC. This behavior can be explained by the influence of the local electronic potential at the surface of the particle on the intercalation current. The potential in turn directly relates to the path length of points at the surface to the contact at the CC. This is reflected by the overpotentials plotted as slice averages in through-direction in Fig. 5e. The overpotentials of the *SPM-ideal* case for high conductivity (solid blue line) always lie above the *SPM-reference* case (dotted red line). Meanwhile, the case with lower conductivity (dashed green line) is clearly tilted and lies below the *SPM-reference* case up to roughly 8 µm. Recall, that the CC is placed at around 12.6 µm. The overpotential average (6.5144e-4 V) is almost identical to the case with high conductivity (6.4878e-4 V). Interestingly, the slice-averaged overpotentials for both cases are very close or below the ones related to the *SPM-reference* case except for the region close to the CC. Then, comparably much higher overpotential can be observed. The maxima are around 2.454 mV for σ_s = 1e-3 S/cm and 4.483 mV for σ_s = 1e-5 S/cm, which is 3.77 and 6.88 times the average value, respectively. Finally, the measured GITT potential depicted in Fig. 5c deviates significantly from the *SPM-reference* case during the pulse phase by around 12.9 mV. The shifted curves in Fig. 5d show that this is mostly a constant offset caused by the bottleneck at the connection to the CC. In addition, another small feature appears in the first couple of seconds during, both, the pulse and relaxation phase, which is well visible in Fig. 5d.

Extracted diffusion.—The resulting extracted solid-state diffusion coefficients and related confidence intervals are listed in Fig. 5f. Impact on the extracted D_{Li} is minor yet the error increases for decreasing conductivity. This is expected, as the impact on the concentration distribution increases for a decreasing conductivity. The effect adds to the implications of surface coverage, which are always present. For the case of high conductivity (1e-3 S/cm), the point-estimate of D_{Li} deviates by only 6% originating from the low amount of covered reactive surface area. This is consistent with the small overall deviation of the measured voltages from the *SPM-reference* case. Increasing ohmic resistances intensify preferential lithiation at the electronic connection. The resulting rapid increase of voltage at the beginning of the pulse artificially increases the square-root slope. At lower conductivities, the point-estimate difference in D_{Li} consequently increases up to 17% at 1e-5 S/cm. The features extracted from the data, cf. Table S6, are consistent with this physical intuition. The additional small feature at the beginning of each GITT phase influences the extracted square-root slopes. At 1e-5 S/cm, $\mathrm{d}U^P/\mathrm{d}\sqrt{t}$ and $\mathrm{d}U^R/\mathrm{d}\sqrt{t}$ and are both increased by 9.5% and 17.1%, respectively.

Influence of secondary particle structure.—Next, we want to investigate the influence of particle cracking on the extracted diffusion coefficient via the *SPM-fractured* case. Similar to the investigation in the previous section, the microstructural influences on the measured GITT curves can be partly separated. Again, this is possible by comparing the results for high and low electronic conductivities.

Effect of extended surface.—For the highest electronic conductivity (σ_s = 1e-3 S/cm), electron transport limitations become negligible. Consequently, effects of an increased particle surface area in conjunction with a reduction of diffusive path lengths for the lithium inside the particle are isolated. Figure 6a depicts the related lithium distribution inside the particle. The lithiation pattern obviously differs from the *SPM-reference* case due to the different particle structure. Nevertheless, the local concentration similarly depends on

the path length to the nearest surface. Reduction of the effective diffusion length is reflected in the related GITT voltage curve in Fig. 6c. Note, that the characteristic diffusion length cannot be described by a single value anymore like in the *SPM-reference* case. Instead, it is characterized by a distribution of values with a mean value below the particle radius. Short diffusion pathways lead to a better utilization of the particle resulting in an overall lower voltage. This is reflected in the related cell voltage, which is depicted as the full blue line in Fig. 6c. The overall deviation of the measured voltage to the reference is at most 7.7 mV.

Similar to the *SPM-ideal* case, the overpotential has a minor effect on the measured potential. It accounts for only around 0.37 mV of the deviation, but scales approximately linearly with the active surface area following the relation discussed in Section S4. At 240 s, the average value of 0.26007 mV is by a factor of 2.4110 lower compared to the *SPM-reference* case independently of conductivity, cf.. Fig. 6e. The surface area is increased by a factor of 2.4670 in comparison.

The main deviation in measured potentials originates from the increased surface concentration. It causes around 7.1 mV of the 7.36 mV at the 240 s of pulse duration presented in Fig. 6. Interestingly, the estimate for the deviation given by Eq. 2 is still able to roughly approximate the influence. It predicts $(1 - 1/2.4670) \cdot 0.0437 \approx 26$ mV, even though the assumptions for the formula are mostly violated.

Effect of conductivity.—The additional influence of conductivity is getting evident for the lowest conductivity $\sigma_s = 1\text{e-}5$ S/cm. The lithiation pattern depicted in Fig. 6b shows a shift of the lithiation toward the current collector similar to the *SPM-ideal* case. However, the effect is much more pronounced. This can be explained by the electronic pathways which become much more tortuous due to the fractures. The related GITT voltage curve in Fig. 6c deviates strongly from the *SPM-reference* case. Nevertheless, it is mostly a constant offset due to ohmic losses as seen in the relaxation phase of the measurement as well as in Fig. 6d during the pulse. Figure 6d also reveals, that in comparison to the *SPM-ideal* case, this has a much more pronounced effect on the short-term behavior. In fact, it counteracts the effect of the shortened diffusive pathways and even dominates the voltage response.

Extracted diffusion.—The influence on the extracted diffusion coefficients is determined by two opposing trends, which can be explained by Fig. 6d. The increased surface area and shortened diffusion pathways lead to a lower square-root slope in the short-term behavior at the start of each phase of the GITT measurement. This strongly increases the extracted point-estimates of D_{Li} to about 3.9 times the reference value for $\sigma_s = 1\text{e-}3$ S/cm, cf. Fig. 6f. The corresponding features extracted from the measurement are stated in Table S6. The related decrease in square-root slope is a factor of about 1.7 for the pulse phase and 3.4 for the relaxation phase. The decrease in the square-root slope is counteracted by conductive effects, which scale with the electronic conductivity. Compared to the reference, the decrease of the fitted square-root slope amounts to factors of 1.6 and 3.1 for $\sigma_s = 1\text{e-}4$ S/cm and 0.65 and 0.35 for $\sigma_s = 1\text{e-}5$ S/cm for the pulse and relaxation phase, respectively. This is consequently reflected in the extracted D_{Li} lowering the point-estimates to 3.8 and 0.23 times the reference for 1e-4 S/cm and 1e-5 S/cm, respectively. Note, that these values were extracted by a fit using the same time interval of 180 s. This could lead to an underestimation of these effects as a shorter time interval would emphasize the short-term behavior, even though it might not follow an ideal square-root-like behavior. This ambiguity when working with actual data was omitted in this analysis by using a unified fit interval for all virtual GITT measurement data.

Influence of electrode microstructure.—For the analysis of transport on the electrode level we focus on two different setups. The *electrode-ideal* case shows effects of an accumulation of many particles of exactly the same size connected by a CBD matrix. The *electrode-PSD* case combines these effects together with particles drawn from a Gaussian random distribution. Details on the particle distribution and sizes are provided in Fig. S4.

Effect of electrode transport.—Due to the high amount of conductive additives, major parts of the particle surfaces in both electrodes are covered by CBD. 10% of the total mass of the electrodes were carbon additives and binders corresponding to around 15 vol% CBD. This leads to 71.45% and 72.91% of the surface being covered by CBD voxels for the *electrode-ideal* case and *electrode-PSD* case, respectively. Due to the model assumption

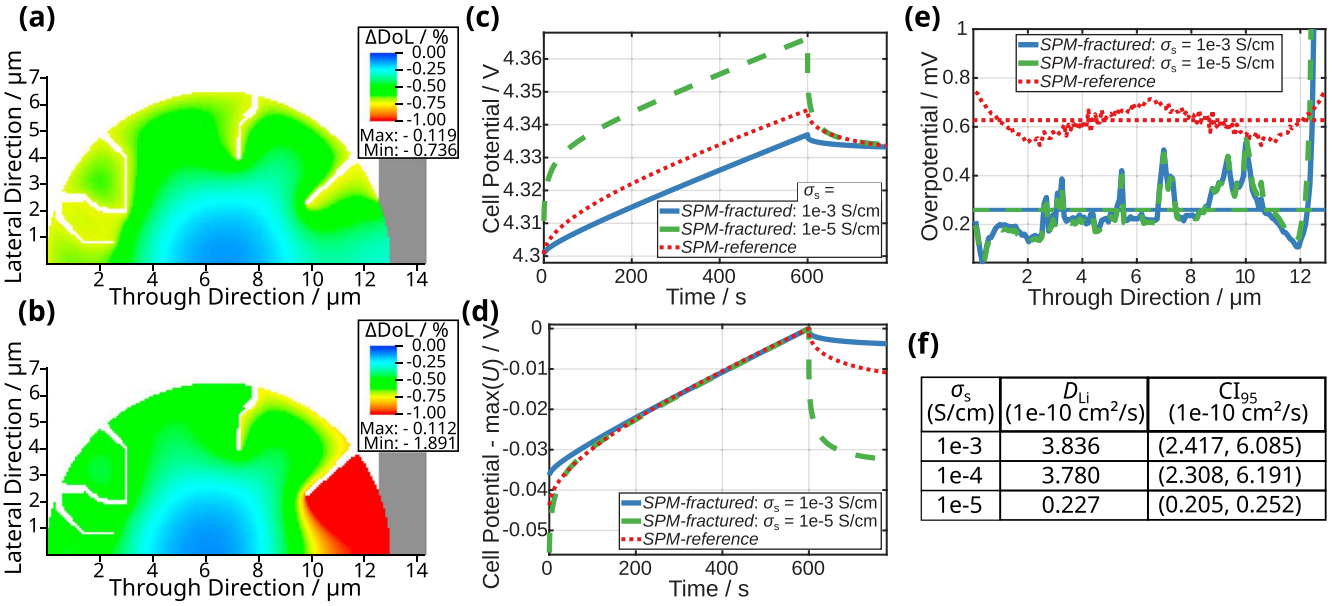

σ_s (S/cm)	D_{Li} (1e-10 cm²/s)	CI_{95} (1e-10 cm²/s)
1e-3	3.836	(2.417, 6.085)
1e-4	3.780	(2.308, 6.191)
1e-5	0.227	(0.205, 0.252)

Figure 6. Influence of secondary particle structure. Results depicted for the *SPM-fractured* case with $D_{Li} = 1\text{e-}10$ cm^2/s. Lithiation pattern within the particle at $t = 240$ s with an average ΔDoL of −0.533% for (a) $\sigma_s = 1\text{e-}3$ S/cm and (b) $\sigma_s = 1\text{e-}5$ S/cm. (c) Resulting cell potentials for the first 780 s of the GITT procedure. (d) Cell potentials shifted by their respective maxima removing constant offsets during the pulse phase. (e) Slice-averaged overpotentials over the through-direction. Horizontal lines indicate global averages. (f) Extracted D_{Li} and 95% confidence CI_{95}.

on the CBD having 50% nanoporosity, the active surface area is reduced by half of that, which means around 36%. In contrast to the *SPM-ideal* case, the CBD does not obstruct diffusional pathways in the AM by completely blocking off parts of the particles' active surface area on the scale considered in this work. The lithiation patterns therefore follow the radially symmetric pattern. Figure 7a illustrates this by depicting exemplary 2D slices through particle centers of the *electrode-PSD* case. The conductive additives improve the overall electrode conductivity to a point, where the influence of the AM conductivity becomes negligible. This can be seen in Fig. 7b as the dashed lines for the low conductivity lie on top of the solid lines representing the high conductivity data. The deviation in cell voltage between the *electrode-ideal* case and the *SPM-reference* case in Fig. 7b during the pulse phase is approximately a constant offset. This becomes evident by the almost perfect overlay of the corresponding voltage curves in Fig. 7c. As a consequence, the *SPM-reference* case shows the same offset in the relaxation phase in Fig. 7c. The magnitude of the constant offset in measured voltages for the *electrode-ideal* case is about 3.58 mV compared to the *SPM-reference* case. It can be explained by the reduced active surface area due to the CBD coverage. The reduced surface area leads to an increase in average overpotential on the one hand and a stronger decrease in surface concentration underneath CBD-covered surfaces on the other.

The average overpotential, indicated by the vertical lines in Fig. 7d, is increased by a factor of 1.7410 and 2.0941 for the *electrode-ideal* case and *electrode-PSD* case, respectively. Note, that this is slightly higher than the fractions of the volumetric surface areas, which are 1.5737 and 1.9006. This is due to the dependency of the intercalation rate on the surface concentration, whose influence scales with the amount of covered surface. A more detailed discussion on this is given in Section S4. The deviation in average overpotentials accounts for 0.464 mV in the *electrode-ideal* case.

The remaining main part of the deviation can be explained by a stronger decrease in surface concentrations at covered areas. Such areas require a higher overpotential to sustain the same average current as uncovered ones. This causes a stronger decrease in surface concentration in turn further shifting the open-circuit potential. The effect can be seen qualitatively in the slice-averaged overpotentials in Fig. 7d, which show higher variances for the electrode cases compared to the reference. Particles close to the separator are covered less by CBD as they have less contact points to other particles. Consequently, this results in lower overpotentials in the first 10 μm of both electrodes.

Effect of particle size distribution.—The effect of a PSD can be seen qualitatively in Fig. 7a. Shorter diffusion lengths of smaller particles lead to a faster increase in their average concentration. The distribution of diffusion lengths results in a changed shape of the measured cell potential throughout the whole measurement procedure which is shown in Fig. 7b. The measured cell potential further reveals that, both, its long- and short-term behavior are altered compared to the reference. Consequently, a noticeable influence on the extracted diffusion constants is expected. Interestingly, all other microstructural phenomena investigated so far only affected the short-term behavior or resulted in an approximately constant offset. Therefore, the effect of a PSD has a unique effect on the measured potential curve making it distinguishable from the other phenomena.

Extracted diffusion.—The resulting extracted solid-state diffusion constants listed in Fig. 7e follow the trends expected from the previous discussion. CBD coverage did not obstruct lithium diffusion in a meaningful way. The reduced reactive surface area consequently lead to an approximately constant offset in measured voltage for the *electrode-ideal* case. Therefore, the extracted D_{Li} also only shows a small point-estimate deviation by less than 4% with a minor variation due to the electronic conductivity. The *electrode-PSD* case influenced, both, the short- and long-term behavior. The distribution of diffusion lengths originating from varying particle radii resulted in an overall bigger slope of the voltage curve. Consequently, the square-root slope increased by around 17.5% (Table S6) reducing the point-estimates of the extracted diffusion by approximately 29%.

Comparison to other evaluation methods.—The previous analysis aimed at establishing links between microstructural features of virtual measurement setups and the resulting D_{Li}. For a more holistic picture, we also want to compare the results to other parameter extraction methods. This will be separated into two parts starting with a general discussion including various selected methods from

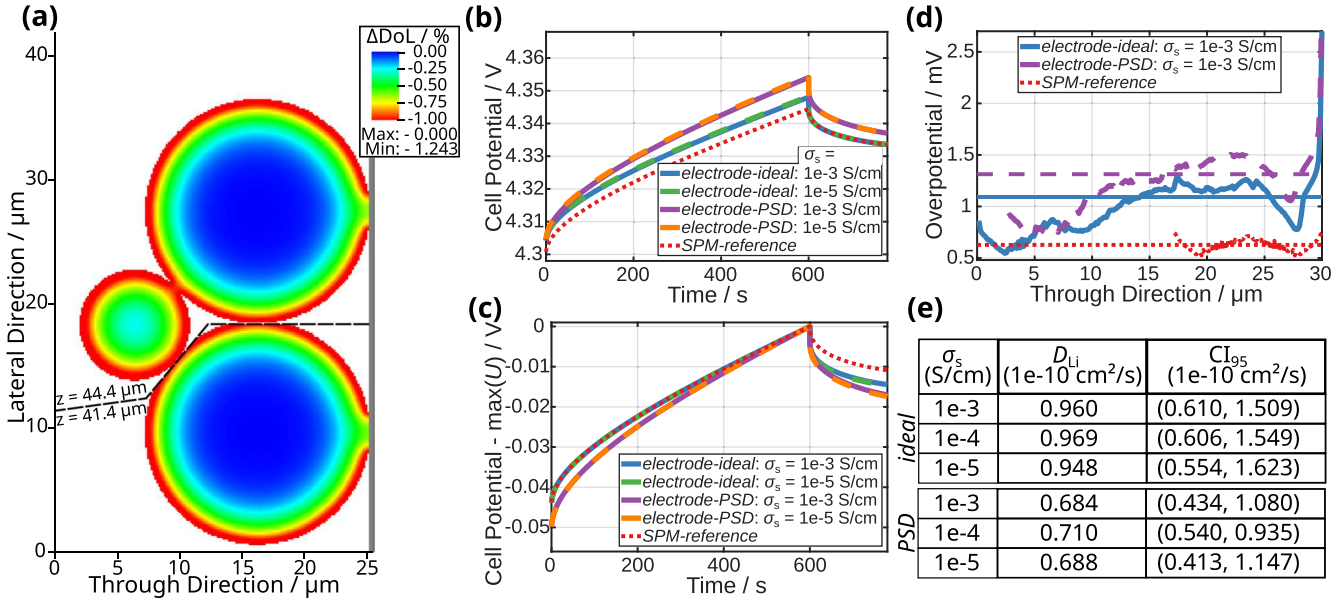

	σ_s (S/cm)	D_{Li} (1e-10 cm²/s)	CI_{95} (1e-10 cm²/s)
ideal	1e-3	0.960	(0.610, 1.509)
	1e-4	0.969	(0.606, 1.549)
	1e-5	0.948	(0.554, 1.623)
PSD	1e-3	0.684	(0.434, 1.080)
	1e-4	0.710	(0.540, 0.935)
	1e-5	0.688	(0.413, 1.147)

Figure 7. Influence of electrode microstructure. Results depicted for the *electrode-ideal* case and *electrode-PSD* case with $D_{\mathrm{Li}} = 1\text{e-}10\ \mathrm{cm}^2/\mathrm{s}$. (a) Lithiation pattern within the *electrode-PSD* case at $t = 240$ s with an average ΔDoL of −0.533% for $\sigma_s = 1\text{e-}4$ S/cm. The top part ($z = 44.4$ μm) cuts through the center of the small particle and the bottom part ($z = 41.4$ μm) cuts through the center of the big particle. (b) Resulting cell potentials for the first 780 s of the GITT procedure. (c) Cell potentials shifted by their respective maxima removing constant offsets during the pulse phase. (d) Slice-averaged overpotentials over the through-direction. Horizontal lines indicate global averages. (e) Extracted D_{Li} and 95% confidence CI_{95}.

literature. Then, the results obtained by EP-BOLFI are compared to ones obtained by applying the extended WH-formula Eq. 1.

General discussion.—For a comparison between different parameter extraction methods, it is important to understand the assumptions and simplifications that they are based on. For clearness, the discussion will be limited to the EP-BOLFI method in conjunction with the herein applied cell-scale simulations via *PyBaMM*. It should be noted, however, that the method is in general not bound to any particular battery model or simulation tool.

The EP-BOLFI method applied within this work uses simulations of a homogenized cell-scale battery model at its core. That is why the method can account for any details resolved by the model assuming the features were chosen accordingly. This includes effects of the electrolyte, counter electrode and electrode tortuosity. In contrast, the model does not account for the microstructural factors investigated within this analysis, but this also extends to other effects like aspherical particles or anisotropic diffusive transport. It is hence important to understand the limitations of the model when applying the method to experimental data.

The extended WH-formula Eq. 1 is based on an analytical solution to the diffusion equation within a spherical particle. It assumes semi-infinite diffusion as well as a constant intercalation current without considering the impact of the local environment on the surface. The exact assumptions and derivation are detailed in Weppner et al.[6] Standard cell-scale models including the SPMe

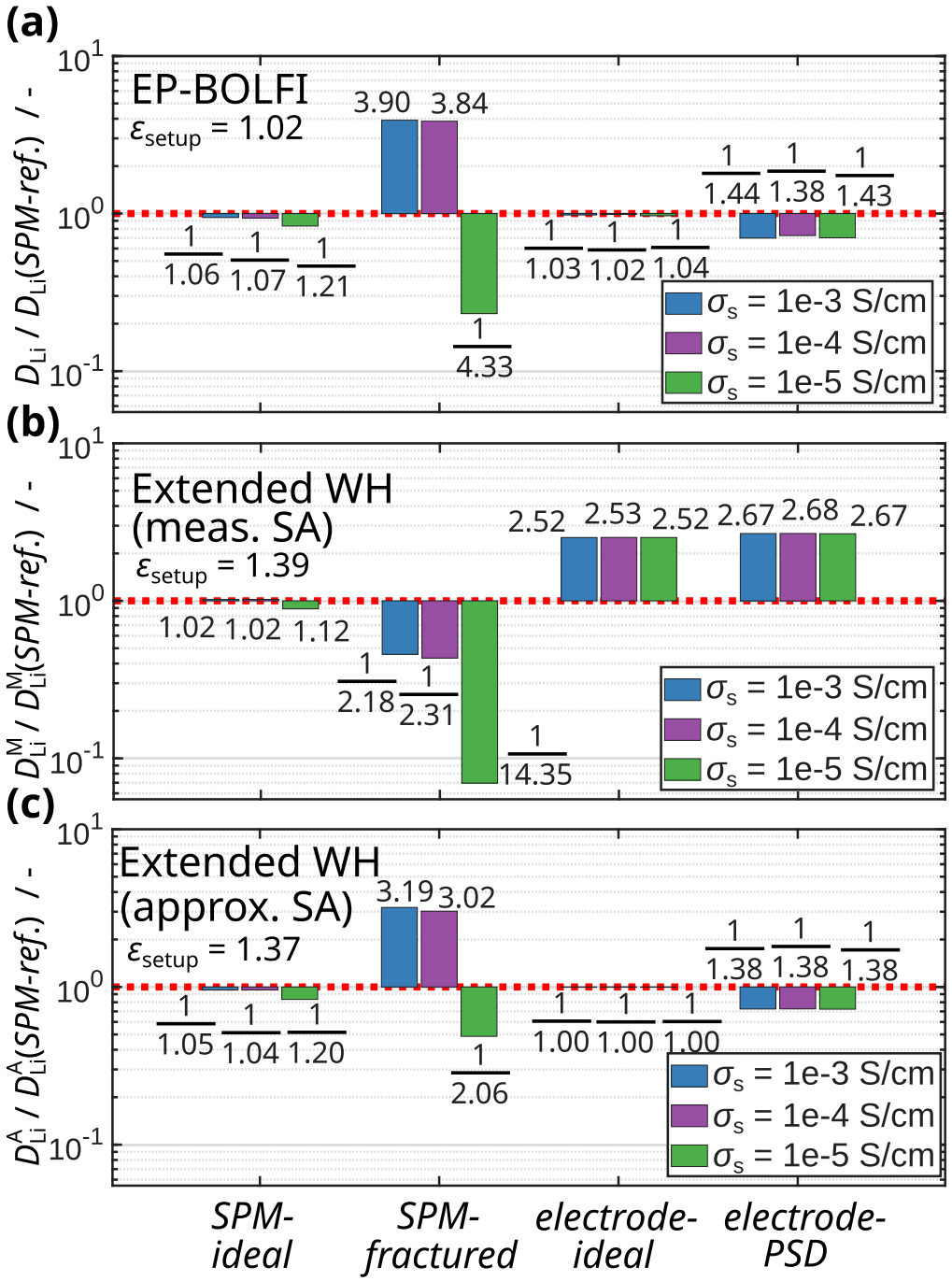

Figure 8. Comparison of the extracted diffusion for an intrinsic diffusivity in the virtual experiment of D_{Li} = 1e-10 cm^2/s. Results for a parameter extraction via (a) EP-BOLFI, (b) the WH-formula with measured active surface areas, and (c) the WH-formula with approximated active surface areas. The intrinsic error ε_{setup} of each method is given by the fraction of the true diffusivity of the material over the extracted D_{Li} for the *SPM-reference* case.

which was applied here solve the diffusion equation for spherical particles as well. As a consequence, cell-scale models predict the same concentration profile during the pulse phase, if the conditions required by the extended WH-formula are met. The extended WH-formula can therefore be interpreted as a simplified approach compared to EP-BOLFI.

The standard WH-formula, also known as 4-point-formula, is a simplification of the extended WH-formula.[6] It additionally assumes, that the cel potential is linear with respect to the square root of time over the whole pulse duration, which in particular requres linearity of the open-circuit potential U_0. The application of the formula is therefore especially critical in regions with significant variations of the slope of U_0.

The ICI method, which was introduced by Chien et al.[8], extracts D_{Li} from short relaxation phases during an otherwise constant applied current. It is based on similar assumptions as the extended WH-formula as well as the same analytical solution to the diffusion equation within a spherical particle. Cell-scale models are thus able to predict matching concentration profiles during a relaxation phase given the conditions for the ICI formula hold. Therefore, the method can also be interpreted as a simplified approach compared to EP-BOLFI.

In summary, the applied EP-BOLFI method can be seen as the most general and flexible approach of the discussed methods. The ICI and extended WH-approach can be considered as simpler approaches and, finally, the 4-point-formula is the most simple method. Note, that also other methods could achieve the same quality of results as EP-BOLFI, given they are based on battery models with a similar level of detail. Naturally, increased accuracy comes with certain expenses as well. Methods based on forward simulations of battery models are computationally more intense, even though this is usually manageable. Further, more precise methods typically become increasingly sophisticated in their application. Note, that this can also be seen as an advantage. The increased complexity requires the user to actively account for the many factors set by experimental boundary conditions and decide on their relevance. For example, determining the square-root slope in order to apply the extended WH-formula would automatically reveal if the measured relation remained linear throughout the whole pulse duration. Hence, it would become directly evident whether an application of the simpler 4-point-formula is justified or not. Conversely, mere application of the 4-point-formula could easily miss a violation of this assumption.

Quantitative comparison of extraction methods.—In this section, we will compare the results for the extraction of D_{Li} based on the extended WH-formula Eq. 1 to the ones obtained by the herein applied EP-BOLFI method. The evaluations are based on the square-root slopes extracted by EP-BOLFI, cf. Table S6, and the results are illustrated in Fig. 8. The exact values of the extracted D_{Li} are listed in Table S9.

The results for measured ($D_{\mathrm{Li}}^{\mathrm{M}}$) and approximated ($D_{\mathrm{Li}}^{\mathrm{A}}$) surface areas are in good agreement for the *SPM-reference* case, but show a higher deviation of the reference compared to EP-BOLFI of around 27%. This deviation originates from two assumptions of the WH-formula. Firstly, the assumed linearity of the open-circuit potential introduces an error in combination with the long pulsing phase of 600 s. Secondly, the approximation requires semi-infinite diffusion for the square-root-like behavior. Chien et al.[8] have shown, that this approximation holds within 5% error for $t < 0.0032 \cdot r_{\mathrm{P}}^2 / D_{\mathrm{Li}} \approx 13.5$ s for $D_{\mathrm{Li}} = 1\text{e-}10\ \mathrm{cm}^2/\mathrm{s}$. The applied fit over the first 180 s is therefore not optimized for the approximation. Here lies an important difference to the EP-BOLFI approach. In the Weppner-Huggins formula, a too long time span for the square-root fit will directly result in a less accurate prediction of D_{Li}. With EP-BOLFI, the simulations by the optimizer should in theory reflect the same mismatch between measurement and fit, if the real measurement conditions are sufficiently matched by the model. Therefore, EP-BOLFI is still able to accurately recover D_{Li} under such conditions, which is reflected in more accurate values for the *SPM-reference* case.

The *SPM-ideal* case shows the same trend as EP-BOLFI with a very minor deviation from the reference.

For the *SPM-fractured* case, the results depend strongly on the utilized surface area, which is obvious from the strong mismatch between the model assumptions and actual fractured microstructure. Interestingly, while $D_{\mathrm{Li}}^{\mathrm{M}}$ is more precise for high conductivities compared to $D_{\mathrm{Li}}^{\mathrm{A}}$, the prediction for low conductivities has the highest deviation of all considered cases. For $\sigma_{\mathrm{s}} = 1\text{e-}3$ S/cm, $D_{\mathrm{Li}}^{\mathrm{M}}$ underpredicts D_{Li} by a factor of 2.18 compared to an overprediction by a factor of 3.19 for the approximated surface area. The lowest conductivity of $\sigma_{\mathrm{s}} = 1\text{e-}5$ S/cm leads to an underprediction by a factor of 2.06 and 14.35 for $D_{\mathrm{Li}}^{\mathrm{A}}$ and $D_{\mathrm{Li}}^{\mathrm{M}}$, respectively. This can be explained by the harsh increase of the square-root slope due to the additional artificial feature introduced by low conductivities for short times. The increase is in turn directly reflected in a proportional reduction of the extracted D_{Li}, as the WH-formula is strongly influenced by the square-root slope. The extreme discrepancy between the different approaches for the surface areas results from the underprediction of surface area in part canceling out some of the overprediction of the square-root slope in the case of $D_{\mathrm{Li}}^{\mathrm{A}}$.

The *electrode-ideal* case and *electrode-PSD* case behave very similar to the point-estimates by EP-BOLFI in the case of approximated surface areas. The approximations deviate by less than 1% from the reference for the monodisperse electrode. In contrast, the results for $D_{\mathrm{Li}}^{\mathrm{M}}$ predict a 2.52 and 2.67 times higher diffusion for the *electrode-ideal* case and *electrode-PSD* case, respectively. The overprediction originates from the CBD-coverage within the electrodes, as it still allows intercalation at covered surface regions. The current density within the electrolyte at the particle surface increases proportional to the surface coverage due to CBD. At the same time, the effective current density within the particle remains similar to a non-covered particle. This results in a wrong prediction of the local ionic current density at the particle surface, which is basis for the surface-area factor within the WH-formula.

In summary, the extended WH-formula leads to overall less accurate predictions of D_{Li} compared to EP-BOLFI. However, the approximations remain close to the correct order of magnitude except for the case of fractured particles. That is, D_{Li} obtained by the WH-formula deviated at most by factors in the range of $10^{\pm 0.43}$, if the *SPM-fractured* case is excluded. In comparison, the point-estimates of EP-BOLFI deviated at most by factors in the range of $10^{\pm 0.16}$. In the case of particle cracking, an accumulation of errors leads to particularly high inaccuracies in the results when measured surface areas are used in the WH-formula. Consequently, it is particularly important to check to which extent particle cracking could occur when working with real experimental data. Only then, high accuracy of results can be ensured. In cases where it is not possible to exclude particle cracking, a robust extraction method like EP-BOLFI is recommended. Nevertheless, even then only a reliable estimate on the order of magnitude of D_{Li} can be expected. Note, that the WH-formula with approximated surface areas also yielded acceptable results with a precision similar to EP-BOLFI in the considered scenarios. As setup errors were a relevant factor for this method, its precision could be further improved though. This could be achieved by a cycling protocol with shorter pulse durations and optimized intervals for the square-root fit following the approach of Kang et al.[15]

Conclusions

The main results can be summarized as follows. The influence of connectivity by means of the *SPM-ideal* case proved to be minor overall. On the one hand, the implicated partial surface coverage of the particle at the connection area had a negligible influence on the measured voltage. This could be reasoned by the low fraction of covered surface area, which was shown to be the main scaling factor

for the differences in the measured voltage. On the other hand, the effects due to a low electronic conductivity lead to the main deviations. Then, a constant offset in the measured voltage as well as an additional feature at the beginning of the pulse phase was introduced. The extracted point-estimates of the solid-state diffusion coefficient D_{Li} deviated by at most 17% in the considered *SPM-ideal* case for the lowest electronic conductivity of 1e-5 S/cm.

Particle cracking lead to the most extreme deviations in measured voltages and extracted D_{Li}. For high conductivities, the extended surface area exposed to the electrolyte combines with a reduced diffusive path lengths for the lithium inside the particle. This lead to a prediction of D_{Li}, whose point-estimate was 3.9 times higher than the reference. The effect of electronic pathways being much more tortuous due to the fractures becomes evident with a decreasing conductivity. This causes similar changes in the measured voltage as the ones originating from the effect of connectivity, but much more pronounced. While the applied parameter extraction method was not affected by the constant offset, the feature at the beginning of the pulse phase reduces the predicted diffusion constant. The magnitude of this effect scales with decreasing conductivity. For the lowest considered conductivity of 1e-5 S/cm, it became a dominating factor in the parameter extraction reducing the point-estimate of D_{Li} to 0.23 times the reference.

The *electrode-ideal* case showed that the virtual measurement on a thin electrode with a high amount of conductive additives is able to predict D_{Li} with a small point-estimate deviation by less than 4%. The prediction was this precise independently of the AM's electronic conductivity as well as in spite of a high surface coverage of the particles reducing their active surface area by around 36%. The implications of a particle size distribution were considered by means of the *electrode-PSD* case. In contrast to the other considered phenomena, the distribution of diffusion lengths resulted in deviations of the measured voltage throughout the whole pulse phase. The extracted point-estimate of D_{Li} decreased by approximately 29% compared to the reference making it the second highest error source.

Overall, the investigation showed that the applied thin electrode and single particle setup are capable of extracting the real diffusivity with only 4% and 17% point-estimate deviation, respectively. This makes the thin electrode the seemingly best choice to extract the solid-state diffusion constant. It has to be noted though, that effects due to calendering were not considered. This includes possible additional surface coverage of particles at the CC or due to inter-particle contact. In addition, calendering could cause deformation of particles or even particle cracking. Especially the latter could increase the deviation significantly as discussed above. These possible downsides can be avoided by using a SPM setup for the measurement. In theory, this can give SPM an edge over measurements on electrodes, especially for materials with a high electronic conductivity as this increases the accuracy of the setup. In the case of $\sigma_{\mathrm{s}} = 1\text{e-}3$ S/cm, the extracted D_{Li} deviated by only 6% from the reference for the considered *SPM-ideal* case.

The comparison to other extraction methods showed that the application of the extended WH-formula yielded results with an only slightly lower precision for most cases. The case of particle cracking, i.e. the *SPM-fractured* case, combined with measured surface areas was an exception underpredicting D_{Li} by a factor of 14.35. Nevertheless, an awareness of the inherent conditions of the experimental setup as well as the applied parameter extraction method is key in obtaining precise and trustworthy results. This favors more general and complex extraction methods, as most state-of-the-art approaches do not quantify their uncertainty. Consequently, an application to data whose experimental conditions are not fully covered by the method can easily go unnoticed falsifying the extracted material property to an unknown extent. For cases with a known discrepancy between the experiment and the extraction method, application of the workflow presented within this work can help quantifying and reducing such unavoidable errors.

Acknowledgments

The authors acknowledge support with computational resources provided by the state of Baden-Württemberg through bwHPC and the German Research Foundation (DFG) through grant no INST 40/575-1 FUGG (JUSTUS 2 cluster). JH and TD are thankful for the funding received by the German Federal Ministry of Education and Research (BMBF) as part of the ExcellBattMat project (FKZ: 03XP0257B). YK and BH acknowledge funding by the European Union's Horizon 2020 research and innovation programme under grant agreement No. 101103997 (DigiBatt). This work contributes to the research performed at CELEST (Center for Electrochemical Energy Storage Ulm-Karlsruhe).

Data Availability

The simulation framework BEST,[28] which was used for the conduction of virtual GITT experiments, is an in-house code developed in collaboration between Fraunhofer ITWM Kaiserslautern and the DLR Institute of Engineering Thermodynamics. The resulting virtual experiment data as well as the 3D simulation geometries are available on Zenodo: https://doi.org/10.5281/zenodo.20744671. The employed Bayesian optimization approach EP-BOLFI for the extraction of solid-state diffusion coefficients from GITT measurement data is available via the open source *Python* library EP-BOLFI: https://doi.org/10.5281/zenodo.6967238 or "pip install ep-bolfi". The required input files and details on the workflow for the parameter extraction via EP-BOLFI are available on Zenodo: https://doi.org/10.5281/zenodo.20744671. Additional data and workflows are provided upon reasonable request.

ORCID

Johannes Hörmann https://orcid.org/0000-0002-4955-1896
Yannick Kuhn https://orcid.org/0000-0002-9019-2290
Simon Hein https://orcid.org/0000-0002-6728-9983
Birger Horstmann https://orcid.org/0000-0002-1500-0578
Timo Danner https://orcid.org/0000-0003-2336-6059
Arnulf Latz https://orcid.org/0000-0003-1449-8172

References

1. X. Lu et al., "Multi-length scale microstructural design of lithium-ion battery electrodes for improved discharge rate performance." *Energy Environ. Sci.*, **14**, 5929 (2021).
2. T. F. Fuller, M. Doyle, and J. Newman, "Simulation and optimization of the dual lithium ion insertion cell." *J. Electrochem. Soc.*, **141**, 1 (1994).
3. A. Latz and J. Zausch, "Thermodynamic consistent transport theory of Li-ion batteries." *J. Power Sources*, **196**, 3296 (2011).
4. A. Latz and J. Zausch, "Thermodynamic derivation of a Butler–Volmer model for intercalation in Li-ion batteries." *Electrochim. Acta*, **110**, 358 (2013).
5. S. G. Marquis, V. Sulzer, R. Timms, C. P. Please, and S. J. Chapman, "An asymptotic derivation of a single particle model with electrolyte." *J. Electrochem. Soc.*, **166**, A3693 (2019).
6. W. Weppner and R. A. Huggins, "Determination of the kinetic parameters of mixed-conducting electrodes and application to the system Li_3Sb." *J. Electrochem. Soc.*, **124**, 1569 (1977).
7. C. J. Wen, B. A. Boukamp, R. A. Huggins, and W. Weppner, "Thermodynamic and mass transport properties of "LiAl"." *J. Electrochem. Soc.*, **126**, 2258 (1979).
8. Y.-C. Chien, H. Liu, A. S. Menon, W. R. Brant, D. Brandell, and M. J. Lacey, "Rapid determination of solid-state diffusion coefficients in Li-based batteries via intermittent current interruption method." *Nat. Commun.*, **14**, 2289 (2023).
9. M. Oldenburger, B. Bedürftig, E. Richter, R. Findeisen, A. Hintennach, and A. Gruhle, "Analysis of low frequency impedance hysteresis of Li-ion cells by time- and frequency domain measurements and its relation to the OCV hysteresis." *J. Energy Storage*, **26**, 101000 (2019).
10. J. Günther, D. Wycisk, R. Siva Dev, A. Fill, K. P. Birke, R. Moos, J. Philipp Schmidt, and M. Oldenburger, "Determination of the solid state diffusion coefficient of Li-ion battery single-phase materials using thin model electrodes." *J. Electrochem. Soc.*, **172**, 030525 (2025).
11. C. Heubner, U. Langklotz, C. Lämmel, M. Schneider, and A. Michaelis, "Electrochemical single-particle measurements of electrode materials for Li-ion batteries: Possibilities, insights and implications for future development." *Electrochim. Acta*, **330**, 135160 (2020).
12. P.-C. Tsai, B. Wen, M. Wolfman, M.-J. Choe, M. S. Pan, L. Su, K. Thornton, J. Cabana, and Y.-M. Chiang, "Single-particle measurements of electrochemical kinetics in NMC and NCA cathodes for Li-ion batteries." *Energy Environ. Sci.*, **11**, 860 (2018).

13. M. Jia, W. Zhang, X. Cai, X. Zhan, L. Hou, C. Yuan, and Z. Guo, "Re-understanding the galvanostatic intermittent titration technique: Pitfalls in evaluation of diffusion coefficients and rational suggestions." *J. Power Sources*, **543**, 231843 (2022).
14. J. Li, F. Yang, X. Xiao, M. W. Verbrugge, and Y.-T. Cheng, "Potentiostatic intermittent titration technique (PITT) for spherical particles with finite interfacial kinetics." *Electrochim. Acta*, **75**, 56 (2012).
15. S. D. Kang and W. C. Chueh, "Galvanostatic intermittent titration technique reinvented: Part I. A critical review." *J. Electrochem. Soc.*, **168**, 120504 (2021).
16. J. S. Horner, G. Whang, D. S. Ashby, I. V. Kolesnichenko, T. N. Lambert, B. S. Dunn, A. A. Talin, and S. A. Roberts, "Electrochemical modeling of GITT measurements for improved solid-state diffusion coefficient evaluation." *ACS Appl. Energy Mater.*, **4**, 11460 (2021).
17. H. A. A. Ali, L. H. Raijmakers, A. Windmüller, H. Tempel, B. Liaw, P. H. Notten, and R.-A. Eichel, "Evaluating the determination of solid-phase diffusion and reaction-rate constant for Li-ion batteries." *J. Energy Storage*, **132**, 117628 (2025).
18. Y. Kuhn, H. Wolf, A. Latz, and B. Horstmann, "Bayesian parameterization of continuum battery models from featurized electrochemical measurements considering noise." *Batter. Supercaps*, **6**, e202200374 (2023).
19. Z. Geng, Y.-C. Chien, M. J. Lacey, T. Thiringer, and D. Brandell, "Validity of solid-state Li^+ diffusion coefficient estimation by electrochemical approaches for lithium-ion batteries." *Electrochim. Acta*, **404**, 139727 (2022).
20. Y. Kuhn, B. Rana, M. Philipp, C. Schmitt, R. Scipioni, E. Flores, D. Kopljar, S. Clark, A. Latz, and B. Horstmann, "Workflows and principles for collaboration and communication in battery research." *Digital Discovery*, **5**, 177 (2026).
21. A. A. Wang et al., "Review of parameterisation and a novel database (LiionDB) for continuum Li-ion battery models." *Prog. Energy*, **4**, 032004 (2022).
22. Z. Xu et al., "Charge distribution guided by grain crystallographic orientations in polycrystalline battery materials." *Nat. Commun.*, **11**, 83 (2020).
23. A. C. Wagner, N. Bohn, H. Geßwein, M. Neumann, M. Osenberg, A. Hilger, I. Manke, V. Schmidt, and J. R. Binder, "Hierarchical structuring of NMC111-cathode materials in lithium-ion batteries: An in-depth study on the influence of primary and secondary particle sizes on electrochemical performance." *ACS Appl. Energy Mater.*, **3**, 12565 (2020).
24. P. Gao, S. Wang, Z. Liu, Y. Jiang, W. Zhou, and Y. Zhu, "Experimental and mechanism research of gradient structured $LiNi_{0.8}Co_{0.1}Mn_{0.1}O_2$ cathode material for Li-ion batteries." *Solid State Ionics*, **357**, 115504 (2020).
25. M. Müller, L. Schneider, N. Bohn, J. R. Binder, and W. Bauer, "Effect of nanostructured and open-porous particle morphology on electrode processing and electrochemical performance of Li-ion batteries." *ACS Appl. Energy Mater.*, **4**, 1993 (2021).
26. R. Ruess, S. Schweidler, H. Hemmelmann, G. Conforto, A. Bielefeld, D. A. Weber, J. Sann, M. T. Elm, and J. Janek, "Influence of NCM particle cracking on kinetics of lithium-ion batteries with liquid or solid electrolyte." *J. Electrochem. Soc.*, **167**, 100532 (2020).
27. M. Chouchane, E. N. Primo, and A. A. Franco, "Mesoscale effects in the extraction of the solid-state lithium diffusion coefficient values of battery active materials: Physical insights from 3D modeling." *J. Phys. Chem. Lett.*, **11**, 2775 (2020).
28. Fraunhofer Institute for Industrial Mathematics (ITWM), BEST—Battery and Electrochemistry Simulation Tool. https://www.itwm.fraunhofer.de/best, Accessed: 2026-03-12.
29. A. Latz and J. Zausch, "Multiscale modeling of lithium ion batteries: Thermal aspects." *Beilstein J. Nanotechnol.*, **6**, 987 (2015).
30. L. S. Kremer, T. Danner, S. Hein, A. Hoffmann, B. Prifling, V. Schmidt, A. Latz, and M. Wohlfahrt-Mehrens, "Influence of the electrolyte salt concentration on the rate capability of ultra-thick NCM 622 electrodes." *Batter. Supercaps*, **3**, 1172 (2020).
31. R. Amin and Y.-M. Chiang, "Characterization of electronic and ionic transport in $Li_{1-x}Ni_{0.33}Mn_{0.33}Co_{0.33}O_2$ (NMC_{333}) and $Li_{1-x}Ni_{0.50}Mn_{0.20}Co_{0.30}O_2$ (NMC_{523}) as a function of Li content." *J. Electrochem. Soc.*, **163**, A1512 (2016).
32. Math2Market, GeoDict. https://www.geodict.com/, Accessed: 2026-03-12.
33. P. Soille, *Morphological image analysis: Principles and applications* (Springer, Berlin Heidelberg) 2nd ed. (2003).
34. B. Prifling et al., "Quantitative comparison of different approaches for reconstructing the carbon-binder domain from tomographic image data of cathodes in lithium-ion batteries and its influence on electrochemical properties." *Energy Technol.*, **11**, 2200784 (2023).
35. J. Landesfeind, J. Hattendorff, A. Ehrl, W. A. Wall, and H. A. Gasteiger, "Tortuosity determination of battery electrodes and separators by impedance spectroscopy." *J. Electrochem. Soc.*, **163**, A1373 (2016).
36. V. Sulzer, S. G. Marquis, R. Timms, M. Robinson, and S. J. Chapman, "Python battery mathematical modelling (PyBaMM)." *J. Open Research Software*, **9**, 14 (2021).
37. Y. Kuhn, M. Adachi, M. Philipp, D. A. Howey, and B. Horstmann, "A primer on Bayesian parameter estimation and model selection for battery simulators." *arXiv* (2025), doi:10.48550/arxiv.2512.10055.